



# Numerical and experimental investigation of pollutant formation and emissions in a full-scale cylindrical heating unit of a condensing gas boiler

Jörn Hinrichs<sup>a,\*</sup>, Daniel Felsmann<sup>a</sup>, Stefan Schweitzer-De Bortoli<sup>b</sup>, Heinz-Jörg Tomczak<sup>b</sup>, Heinz Pitsch<sup>a</sup>

<sup>a</sup> RWTH Aachen University, Institute for Combustion Technology, Templergraben 64, 52056 Aachen, Germany

<sup>b</sup> Vaillant GmbH, Berghauser Straße 40, 42859 Remscheid, Germany

## HIGHLIGHTS

- Detailed numerical and experimental study of a full-scale condensing gas boiler.
- Identified high emission regions due to locally varying burnt temperature levels.
- CO emissions are caused by a freeze of CO oxidation due to a steep cooling gradient.
- Majority of NO is formed within the flame front and not in post flame region.

## ARTICLE INFO

### Keywords:

Condensing gas boiler  
Premixed lean laminar combustion  
CO  
NO<sub>x</sub>  
Resolved simulation  
Experimental measurements

## ABSTRACT

The condensing gas boiler technology has received increasing attention due to its very high efficiency of more than 90%, which is an increase of more than 15% compared to non-condensing boiler devices. With this, condensing gas boilers offer the chance to decrease the energy consumption and CO<sub>2</sub> emissions for domestic hot water and heating. While further increasing the energy efficiency of condensing boiler devices, pollutant emissions have to be considered as well since they are a threat to human health and therefore subject to continuously intensified governmental restrictions. In this study, a comprehensive investigation of the full-scale heating unit of a commercial condensing gas boiler was performed. Local measurements at different axial positions revealed an inhomogeneous distribution of CO and NO emissions due to varying temperature levels in the burnt region. Resolved simulations with finite rate chemistry identified a quenching of the CO oxidation reactions due to a fast depletion of OH radicals. Consequently, the CO concentration in the cooled exhaust gas is significantly higher than expected from chemical equilibrium calculations. Regarding NO formation, the majority of NO is found to be produced within the flame front, while only a small part is formed in the postflame region. A detailed pathway analysis pointed out that besides the well known thermal NO pathway, the NNH pathway has the highest contribution to the overall NO emissions. These insights open up possibilities to develop new condensing boiler generations where emission levels below the permitted limits can be achieved.

## 1. Introduction

Providing energy for domestic hot water and heating accounts for one third of the total energy consumption in Europe [1]. Here, natural gas represents the main energy source with a share of roughly 80% [1]. To generate heat from natural gas, condensing gas boilers are state of the art and their market share is continuously increasing in Europe, China, and the United States [2–4]. This boiler generation is more efficient than previous non-condensing heating devices, because the latent heat of the water vapor in the flue gas is exploited by condensation

[2]. With this, energy efficiency levels of up to 115% with respect to the lower heating value can be obtained [5]. Such high efficiency levels enable noteworthy gas fuel consumption savings along with a massive reduction of CO<sub>2</sub> emissions, which possess a significant global warming potential [1]. Despite these achievements, further steps are planned to decrease CO<sub>2</sub> emission levels in condensing gas boiler devices. By adding hydrogen to the natural gas network, the carbon content of the fuel and consequently the CO<sub>2</sub> concentration in the flue gas can be decreased significantly [6]. The condensing gas boiler technology can also support the energy transition towards renewable energy sources,

\* Corresponding author.

E-mail address: [J.Hinrichs@itv.rwth-aachen.de](mailto:J.Hinrichs@itv.rwth-aachen.de) (J. Hinrichs).

<https://doi.org/10.1016/j.apenergy.2018.08.011>

Received 29 May 2018; Received in revised form 23 July 2018; Accepted 3 August 2018

Available online 22 August 2018

0306-2619/ © 2018 Elsevier Ltd. All rights reserved.

because power-to-gas processes represent a method to store the intermittent solar and wind energy sources by producing gaseous fuels like hydrogen or methane, which are then fed into the natural gas network [7].

While developing new condensing gas boiler generations, emission levels of carbon monoxide (CO) and nitrogen oxides ( $\text{NO}_x$ ) have to be considered as well. These species contribute to the ozone depletion and in higher concentrations are highly dangerous to human health [8,9]. On this account, legal regulations, such as the European norm DIN EN 15502-1 [10,11], were established and emission limits have become continuously stricter since then. To achieve such low-emission characteristics, different types of condensing gas boiler devices exist, mainly characterized by the burner geometry that stabilizes the laminar premixed flame.

Porous media burners, such as ceramic foam or metal fiber burners, received much attention recently [12–17] in an attempt to effectively decrease NO and CO emissions by employing a radiant mode [13]. Malico et al. [14] studied the effect of high flame heat losses to a porous media burner and its reducing effect on the course of CO and NO emissions. They compared numerical results to experiments of Trimis et al. [12] and found their model to underpredict CO and overpredict NO emission levels. The drawback of increasing heat losses to the burner is the simultaneously increasing thermal load of the burner material, which reduces the lifetime and increases the material costs of the boiler.

Besides porous media burners, perforated burner plates have been investigated. Here, focus was on stabilization and blowoff limits [18], burner velocity profiles [19], and the effect of varying pressure levels on the flame surface area [20]. Only a few investigations on cylindrical multi-hole burner plates have been carried out, mainly discussing geometry optimization in order to improve the system efficiency [21,22].

Regarding the formation of carbon monoxide and nitrogen oxide, Bouma et al. [13] pointed out that reducing the flame temperature by using leaner mixtures decreases CO and NO concentration in the exhaust gas simultaneously. However, this measure is limited to flammability and blowoff limits and commercial boiler devices are already operated under lean conditions.

Lee et al. [23] studied numerically the effect of different burner-to-coil distances on the CO and  $\text{NO}_x$  emissions. In their optimized model, one coil package was positioned relatively close behind the flame front to cool the flue gas below the NO critical temperature. A second cooling stage was positioned further downstream to improve the CO oxidation.

These studies focused on selected or idealized aspects of condensing boiler devices. They provide knowledge on how effective various measures are in reducing emissions. However, the reasons on a mechanistic level, which are important for reduction of such pollutants, have not been discussed. Consequently, the aim of this study is to analyze a full-scale condensing boiler system with detailed experimental and numerical methods. With this, the important processes

leading to emissions of CO and NO should be identified and suggestions to further decreasing emission levels will be derived.

In condensing gas boilers, the hot flue gas is rapidly cooled down by the heat exchanger. This causes a fast depletion of OH radicals and consequently a freezing of the CO oxidation reaction, which has been investigated more fundamentally in a simplified setup by Creighton [24]. This CO oxidation freezing can be expected to be the dominating cause for CO emissions in condensing gas boilers. However, this effect has never been analyzed in detail in a full-scale system. With regard to the NO emissions of condensing gas boiler devices, the nowadays standard operation under lean conditions has already decreased burnt gas temperatures and NO emission levels simultaneously. However, lower temperatures in the postflame region reduce the importance of the thermal NO formation pathway [25]. Consequently, other NO formation pathways like the NNH-, the  $\text{N}_2\text{O}$ , or the prompt NO mechanism become more relevant. This is a crucial aspect, since the strategies for avoiding NO from these sources are not as straightforward as for thermal NO.

In this study, radial profiles of the interesting quantities CO, NO, and temperature along the pathway from the cylindrical multi-hole burner surface through the cylindrical cooling coils were extracted. Temperature was measured using a thermocouple, while species measurements were performed utilizing probe sampling coupled to a gas chromatograph (GC) and a chemiluminescence detector (CLD). To study the homogeneity of the full-scale heating unit, these radial measurements were repeated at several axial positions. To gain further understanding of the CO and NO formation, resolved simulations utilizing detailed chemical kinetics were performed and numerical results were compared to the experimental data. The availability of radical concentrations in the simulation allowed a deeper analysis of the CO oxidation freezing at flue gas cooling and a detailed NO formation pathway analysis according to the method of Trisjono et al. [26].

This paper is organized as follows: in Section 2, the setup of the cylindrical heating unit and the applied measurement techniques are explained. The numerical framework of the resolved simulations is summarized in Section 3. Section 4 outlines the experimental results of the temperature and species measurements, before in Section 5, numerical and experimental results are compared and discussed. Finally, conclusions are drawn and steps for future work are suggested in Section 6.

## 2. Experimental methods

### 2.1. Burner setup

The investigated cylindrical heating unit is shown in Fig. 1. It was taken from a commercial, condensing boiler, which was modified to enable radial profile measurements of temperature as well as CO and NO concentrations. The heating unit – consisting of burner and cooling coils – was separated from the burner housing to make it accessible for

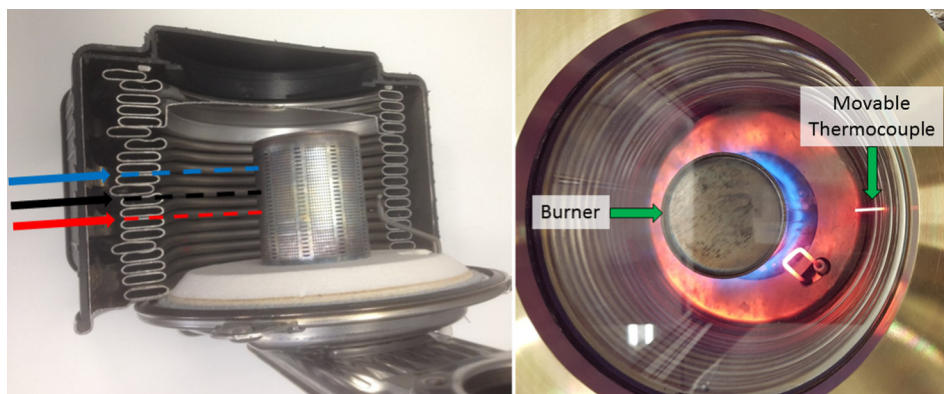


**Fig. 1.** Photos of the utilized cylindrical heating unit. Left: Cross-sectional view of the standard serial produced device consisting of burner, combustion area, cooling coils, gas mixing arm, and housing along with the upper (blue), center (black) and lower (red) axial measurement position. Right: Modified heating unit applied in the present study. (For interpretation of the references to colour in this figure legend, the reader is referred to the web version of this article.)

experimental measurements. In order to minimize buoyancy effects in this partly open setup, the burner is installed in upright position and a quartz glass window was mounted on top of the cooling coils to close the combustion chamber in axial direction. Besides, the quartz glass window allows for optical access as can be seen on the right of Fig. 1.

To provide conditions close to practical operation, fuel and air were supplied through the original gas mixing arm. In the mixing arm, air was metered with a mass flow sensor and methane, which was used as surrogate fuel for natural gas, was added via a stepper motor valve controlled by the commercial control unit. All experiments were carried out at a fixed load point of 25.2 kW, which showed highest load-normalized CO and NO emissions in the exhaust gas under regular operating conditions. In- and outlets of the cooling coils were connected to a heat exchanger that allowed for controlled process water temperature with a spread of 15 K (In/Out: 333/348 K) at 19.75 L/min and 2.5 bar line pressure. Radial profiles were taken at three different axial positions through the gaps between the cooling coils. Axial positions are 28 mm (upper), 52 mm (center), and 81 mm (lower) below the upper lid of the cylindrical flame holder. The original coil gaps were widened to 1.6 mm to ensure sufficient access and an accurate positioning of all probes within the combustion chamber.

## 2.2. Temperature measurements

The temperature measurements were performed with a sheathed B-type (THERMOEXPERT) thermocouple with a diameter of 1 mm. The thermocouple was inserted into the combustion chamber through the widened gap between two cooling coils. To obtain temperature profiles, the thermocouple was radially displaced from the flame holder towards the cooling coils. The temperature was recorded by a calibrated Data-Aquisition-Module (NATIONAL INSTRUMENTS cNI-DAQ-9174/NI 9211), where at each measurement location, the temperature was averaged over 30 samples recorded in a period of 30 s.

It is well known, that thermocouple measurements in hot environments suffer from several error sources that have to be accounted for. In particular, radiative heat losses of the thermocouple bias the measurement towards lower values. The red glowing thermocouple in Fig. 1 demonstrates the significance of thermal radiation. Moreover, the specific configuration in this study, where the thermocouple wires are introduced through the cold cooling coils, require to account also for heat conduction effect from the hot thermocouple junction along the wires towards the cold coils. Therefore, the actual temperature  $T_{corr}$  was calculated using correction terms for radiative and conductive effects to the measured temperature  $T_m$ :

$$T_{corr} = T_m + T_{rad} + T_{cond}. \quad (1)$$

Shaddix et al. [27] derived the energy equation at the thermocouple tip by summing radiative, catalytic, convective and conductive heat loss terms. Since measurement errors due to catalytic effects and heat conduction are very difficult to quantify, thermocouples and test benches are generally designed in a way to minimize these terms. By neglecting both effects, they derived the convective-radiative balance equation:

$$T_{rad} = \epsilon \cdot \sigma \cdot (T_m^4 - T_{coil}^4) \cdot \frac{d_{tc}}{k \cdot Nu}, \quad (2)$$

which compensates for the radiative heat loss effect in the measured temperature. Here,  $\epsilon$  is the emissivity of the thermocouple [28],  $T_{coil}$  is the average coil temperature,  $d_{tc}$  is the diameter of the thermocouple tip,  $k$  is the thermal conductivity of the burnt gas and  $Nu$  is the Nusselt number. Within the current study,  $Nu$  was derived from the resolved simulation for each radial position.

The heat loss along the sheath of the thermocouple was taken into account by considering conductive heat transfer along a circular pin. From this, a correction term  $T_{cond}$  was derived:

$$T_{cond} = \frac{A_c}{A_s} \cdot \frac{k_{tc}}{h_l} \cdot m \cdot T_{coil} \cdot \tanh(m \cdot l_{tc}), \quad (3)$$

where  $A_c$  and  $A_s$  represent the cross section and the surface of the thermocouple, respectively.  $k_{tc}$  is the conductivity of the sheath material,  $h_l$  the convection coefficient, and  $l_{tc}$  the insertion length of the thermocouple into the combustion chamber relative to the coil entrance. A comparison of measured, radiation corrected and conduction corrected temperature can be found in the supplemental material (Fig. 19). The uncertainty level of the radiation corrected temperature was calculated to be up to  $\pm 80$  K, based on error assumptions for the measured temperature (0.5%),  $\epsilon$  (10%),  $k$  (10%), and  $Nu$  (10%).

## 2.3. Species measurements

In order to measure radial species profiles of CO and NO, a deactivated stainless steel tubing (1/16"  $\times$  1.0 mm ID) was utilized for gas sampling purposes. The CO measurements were performed with an Agilent 6890N gas chromatograph (GC) equipped with several detectors and columns. The deactivated stainless steel tubing was connected to a 5 mL sampling loop attached to the GC. To assure that the same amount of matter is introduced into the GC at each realization, the loop was evacuated to 5 mbar and filled with the gas sample to 125 mbar (measured by an Oerlikon Thermovac 101 piezo/pirani pressure gauge). A calibration gas mixture with known composition was used as a reference to accurately quantify the species signals obtained during the measurements. To separate the gas sample, it was forwarded onto a Restek Plot-Q, followed by a Restek molsieve using helium as carrier gas. This combination of columns enabled the separation of CO from other combustion gases like  $O_2$ ,  $N_2$ , and  $H_2O$ . Since low mole fractions ranging between 25 and 350 ppm were expected for CO, a flame ionization detector (FID) coupled with a methanizer was used for quantification. In conventional gas chromatographs, CO can only be detected by a thermal conductivity detector (TCD), but by passing the gas sample through the methanizer, CO is converted to methane and can be detected by the FID. Since the FID is more sensitive (by a factor of 100) than a TCD, this method is preferable for the detection of the CO trace [29].

To quantify the measured signal, a calibration mixture of 100 ppm CO in  $N_2$  was used. The sampling pressure was controlled manually, hence a correction between the calibration pressure and the sampling pressure was considered in the quantification process, following

$$x_{CO} = \frac{S_{CO}}{S_{cal}} \cdot \frac{p_{cal}}{p_{CO}} \cdot x_{cal}. \quad (4)$$

Here,  $S$  is the integrated signal,  $p$  the sampling pressures,  $x$  the mole fraction and the subscripts  $CO$  and  $cal$  denote the measurement and the calibration sample, respectively. Error propagation has been performed based on errors of the signal integration (3%), the calibration gas composition (2%), and the sampling pressures (3% of abs. value). Thereby, the error was determined to be a maximum of 3% of the measured signal. Due to long measurement times of 30 min, 3 measurements per position have been performed. It has to be noted that the effect of CO oxidation freezing through rapid cooling, as reported by Creighton [24], was the target of the investigation. Due to this and the excessive time requirement of the measurement technique, measurements were performed from 44 mm until the CO concentration reaches a constant value.

To perform NO measurements, the same movable stainless steel tubing was connected to a chemiluminescence NO detector (Cambustion CLD 500), which was calibrated with a gas mixture of 90 ppm NO in  $N_2$  directly before each measurement run. Due to the fast measurement interval of 5 ms, an average of 4000 single measurements was performed for each radial position. The error for these measurements arises from the variance of averaging and was found to be  $\pm 4$  ppm as maximum deviation.



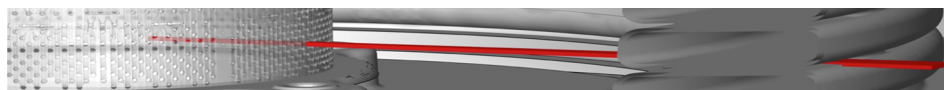


Fig. 2. Section of the considered heating unit consisting of the cylindrical multi-hole burner and the surrounding cooling coil package. The cylindrical simulation domain of a single burner hole is highlighted in red. (For interpretation of the references to colour in this figure legend, the reader is referred to the web version of this article.)

### 3. Numerical framework

#### 3.1. Simulation domain and grid

For a deeper understanding of the CO and NO formation, resolved simulations including finite rate chemistry along the measured pathway were performed. For this, the in-house simulation code CIAO of the Institute for Combustion Technology was used [30]. Within the simulation, a single hole of the cylindrical multi-hole burner is regarded, where the domain starts in front of the burner hole and ends behind the cooling coils as illustrated in red in Fig. 2.

To estimate the flame thickness prior to the resolved simulations, 1D simulations of an unstretched premixed flame were performed. From this, the resolution of the flame region was derived with 40 cells along the flame front, which is much more resolved than in typical literature studies, where only 10–20 cells are used [26]. Besides, the burner hole represents an important length scale, which needs to be resolved accurately. To achieve grid independent results of the flow field, coldflow simulations have been performed beforehand. Here, a grid resolution of 60 cells along the burner hole diameter, i.e. a minimum cell length of 10  $\mu\text{m}$ , was determined to resolve the burner hole.

To reduce the number of cells, the cylindrical mesh only considers half of the hole geometry due to symmetry in axial direction, which results in 6.32 million cells. The part of the grid in the area of the burner hole is displayed in Fig. 3. Further details of the simulation are listed in Table 1.

To enable sensitivity studies with moderate computing time requirements, an attempt was made to represent the circular burner hole by a slot, whose width allows for the same mass flux. This abstraction then allows to neglect the resolution of the circumferential direction and reduces the number of grid cells from 6.32 million to 63,200 cells. The validity of this abstraction from the accurate representation of the burner hole to a slot is verified in Section 5. The resulting two-dimensional grid of the slot case is displayed in Fig. 4 and the local grid size in radial and axial direction, which is identical for the circular hole and the slot case, is plotted in Fig. 5.

#### 3.2. Boundary conditions

The incoming unburnt gas is specified as a premixed methane-air mixture with an equivalence ratio  $\Phi = 0.8$  at a temperature of  $T_u = 298$  K. The inlet velocity, which could not be determined experimentally, is extracted from a cold flow RANS simulation performed with the commercial software ANSYS Fluent. Here, the complete flame holder is modeled as a porous medium, since resolving each hole by the numerical grid is computationally too expensive. At the considered

Table 1

Details of the three-dimensional numerical grid.

Grid points $N_{ax} \times N_{rad} \times N_{cir}$	$69 \times 931 \times 101$
Number of grid cells	6.32 million
Burner hole resolution	$d_{hole}/dx = 60$
Flame resolution	$l_f/dx = 40$
Time step size	$dt = 1.25 \cdot 10^{-6}$ s
Computational cost	0.45 million CPUh

axial burner heights, the inlet gas velocity was determined to 0.227 m/s, 0.349 m/s, and 0.318 m/s at the lower, center, and upper position, respectively.

It can be expected that varying burner exit velocities lead to different lift-off lengths and consequently cause different wall heat losses. This finally leads to different burner surface temperatures, which has also been observed in previous experiments. Initially, the burner surface temperature is approximated to be 600 K based on experiments from the burner manufacturer for this load point. The effect of varying burner temperatures is investigated in Section 5.3.

Symmetry conditions are specified in axial direction and periodicity is applied in circumferential direction. The cooling coil temperature is derived from experimental measurements and is approximated to be a constant value of  $T_{coil} = 473$  K along the coils. This constant temperature boundary condition of the coils was justified by conjugate heat transfer simulations, where only temperature variations of 10–20 K along the solid material occurred due to its high thermal conductivity. The ambient pressure in the domain is set to  $P_{amb} = 1.013$  bar. The boundary conditions, which are fixed for all simulations, are summarized in Table 2.

#### 3.3. Governing equations

In order to represent the laminar burner-stabilized flame within the simulation, the Navier-Stokes equations in cylindrical formulation are solved in the low-Mach number limit as described by Desjardins et al. [30]. The used chemical mechanism consists of 32 species and 213 reactions and was reduced for the oxidation of lean methane flames from a detailed mechanism for high-temperature combustion of engine-relevant fuels [31]. The mechanism was used by Trisjono et al. [26], who indicated that the methane part of the mechanism is very similar to the GRI 3.0 mechanism [32] with only a few updated rates. Regarding the CO oxidation, Creighton [24] states that the reaction



is mainly responsible for the CO oxidation. When the hot flue gas is cooled down by the cooling coils, several recombination reactions like

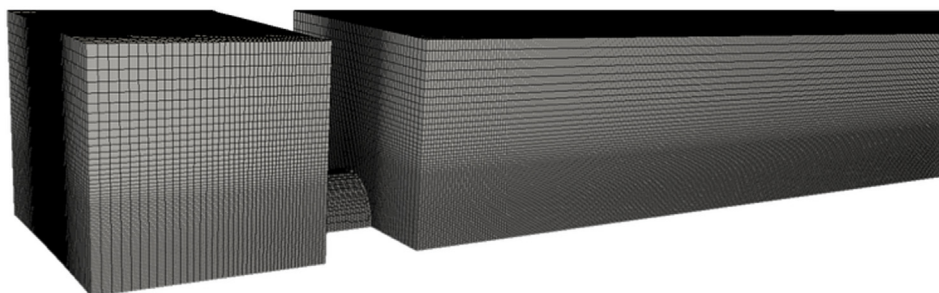


Fig. 3. Section of the simulation grid close to the burner surface of the circular burner hole case.

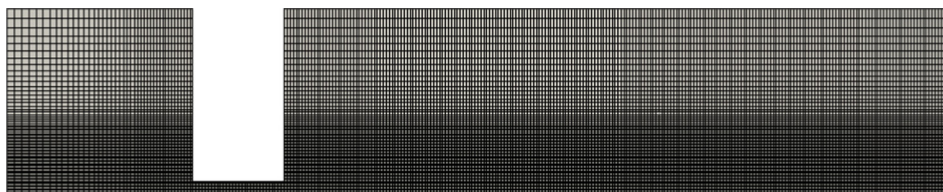
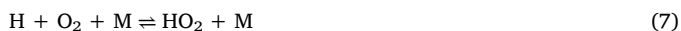


Fig. 4. Section of simulation grid of the slot representation of the circular burner hole.



deplete the available radicals, which then causes a freeze of the CO oxidation reaction [24]. These reactions are contained in the mechanism. Regarding the NO formation, the NO reactions from the GRI 2.11 mechanism are extracted [33].

Within the species transport equations, diffusivity is derived from the unity Lewis number assumption and species diffusion due to temperature gradients (Soret effect) is neglected. In the Navier-Stokes equations, thermal conduction due to species gradients (Dufour effect) as well as heating due to viscous dissipation are neglected.

In order to study radiation heat losses, the optical thin gas (OTG) model is used and compared to the more detailed discrete ordinate (DO) method by Liu et al. [34]. To discretize the spectral dimension, the DO model utilizes the statistical narrow-band-based correlated-k (SNBCK) method. Here,  $\text{CO}_2$ , CO, and  $\text{H}_2\text{O}$  are treated as nongray radiating species, which undergo radiative emission, absorption and are exposed to radiation beam scattering [34]. The DO model is far too expensive to be applied to a three-dimensional simulation. As a consequence, the DO model is only used within the two-dimensional slot configuration case.

### 3.4. Numerical methods

The in-house code CIAO is based on the finite-differences approach and uses a staggered formulation in time and space to improve the accuracy of interpolation stencils and time integration [30]. The semi-implicit time integration is done by a Crank-Nicolson time advancement scheme, while the temperature and species equations are advanced after introducing a symmetric operator split of Strang [35]. The chemical source terms are determined using the implicit backward difference method of the ODE solver package CVODE [36]. The Poisson equation for the pressure is solved by the multi-grid HYPRE solver [37]. Momentum equations are spatially discretized with a fourth order scheme, while scalar equations are discretized with the WENO5 scheme [38].

### 3.5. NO formation pathway analysis

Regarding the NO formation, four pathways can be distinguished, namely the thermal NO, the prompt NO, the NNH and the  $\text{N}_2\text{O}$ -intermediate mechanism [25]. In order to analyze the contribution of the

Table 2

Boundary conditions used in all simulation cases.

$\Phi$	$T_u$	$T_{\text{coil}}$	$P_{\text{amb}}$
0.8	298 K	473 K	1.013 bar

different NO formation pathways, the procedure of Trisjono et al. [26] is applied. For this, the net consumption rate of nitrogen is split into four contributions that each belong to one of the formation pathways listed above. Assuming steady state for all species involved in the NO formation except of  $\text{N}_2$ , NO, and  $\text{N}_2\text{O}$ , the four net consumption rates of nitrogen represent the net NO formation rates via these four pathways.

## 4. Experimental results

Even though the burner stabilized flames are laminar and the methane-air mixture is premixed, the present system cannot be expected to be completely homogeneous. Baffle plates inside the burner create a special flow pattern, which causes spatial varying gas exit velocities at the burner holes. Lee et al. [22] confirmed that for their burner type the unburnt mixture leaves the burner holes with different velocities, which led to different lift-off lengths. In case of higher lift-off lengths, the heat transfer from the flame to the burner surface is reduced, leading to higher flame and reduced burner surface temperatures. The effect of wall heat losses to the burner surface is partially compensated by preheating the unburnt mixture. In the investigated heating unit, it is expected that the wall heat losses and the preheating flux are not completely balancing each other – as it is the case for so called Heat Flux Burners used by several authors [39,40,20] – due to heat fluxes within the solid burner material.

### 4.1. Repeatability of temperature measurements

In order to investigate the repeatability of the measurements, the temperature profiles at the center position of the burner have been recorded four times. Results are illustrated in Fig. 6. All four realizations show a steep rise in temperature close to the burner between 0 and 6 mm, a constant temperature throughout the burnt gas area at 8–50 mm, and a rapid drop of temperature starting from 50 mm due to cooling of the hot flue gas, just before it reaches the cooling coils at 60 mm. The deviations between different realizations are small, but occasionally exceed the error limits calculated from the correction

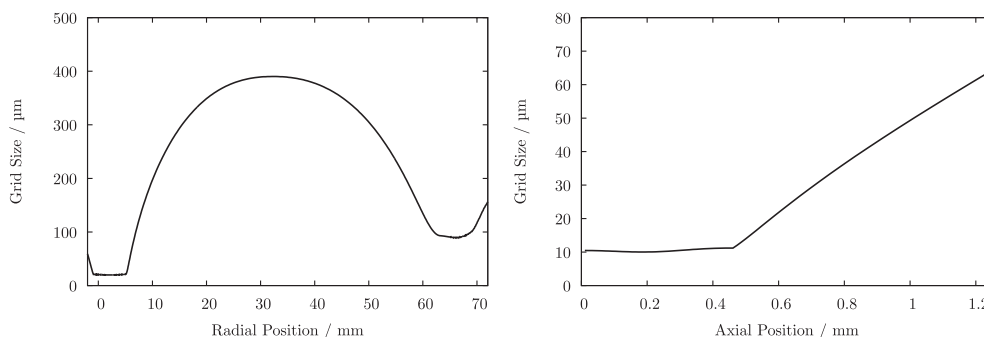
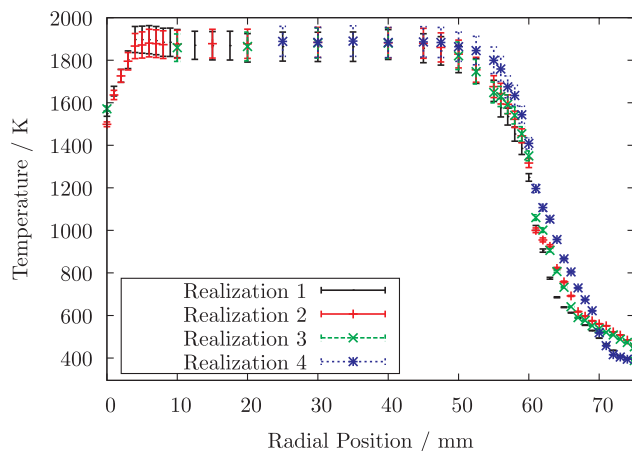


Fig. 5. Left: Grid size in radial direction. Right: Grid size in axial direction.



**Fig. 6.** Different realizations of radial temperature profiles with error bars from radiation and conduction correction at center position (52 mm). Burner surface at 0 mm and cooling coil entrance at 60 mm.

procedure. Close to the burner surface, the slope of all realizations is similar, but the absolute values vary from 1500 to 1570 K, which indicates a high sensitivity of the thermocouple positioning. Besides, the deviation is also caused by the thermocouple diameter of 1 mm, which exceeds the burner hole diameter of 0.6 mm. Thus, an accurate resolution of gradients in axial direction close to the flame holder cannot be obtained.

At 6 mm away from the burner surface, the peak temperature of the radial profile was measured with a value of 1900 K. In the postflame region, the temperature remains constant on that level, which demonstrates that radiative heat losses in the burnt gas do not play a major role. This finding is in contrast to other publications like [14–16], where gas radiation was noted as an important effect. The reason for this insensitivity is the closed system design, which separates the hot flue gas from the cold environment.

When the flue gas enters the cooling coil gap at 60 mm, the temperature curves widen up and show a maximum variance of 192 K at 64 mm, although performed under exactly the same nominal conditions. These observed differences in repeated measurements arise again from uncertainties in accurately positioning the thermocouple in radial direction, which leads to noteworthy deviations in regions with high temperature gradients. Secondly, the temperature measurements are disturbed by the conductive heat loss effect inside the thermocouple, which is already considered in the correction procedure. However, this heat loss effect is amplified, when the thermocouple comes into direct contact with the cooling coils, which is hardly avoidable, since the 1 mm thermocouple is inserted through the 1.6 mm gap between the coils.

Incorporating uncertainties originating from non-avoidable systematic and constructional factors was mandatory to obtain a reliable analysis of the system. Hence, the following radial profiles – if not stated otherwise – were acquired by an average of a minimum of three single measurements and standard deviation errors have been added to the method-depending systematic errors.

#### 4.2. Homogeneity of the heating unit

Temperature profiles have been measured at three different locations to evaluate the spatial homogeneity of the system and the results are presented in Fig. 7. Close to the burner surface, the temperature rise at all three positions is comparable, but the maximum temperature is shifted slightly closer to the burner for the lowest axial position. This observation indicates a smaller lift-off distance of the flame for the lower axial position, which might be related to inhomogeneous exit velocities. As expected, this smaller lift-off length causes an increased

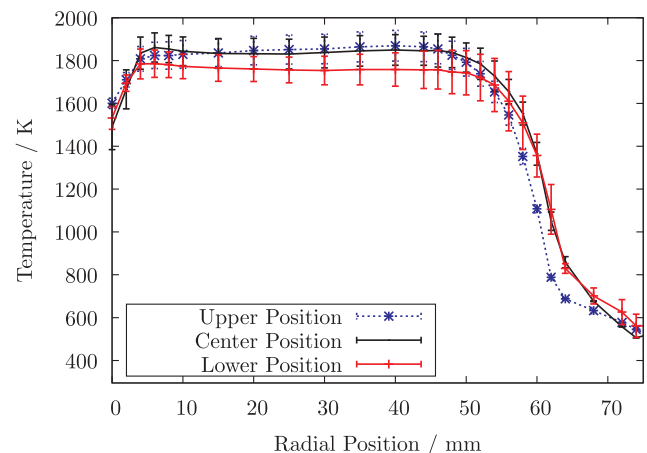


**Fig. 7.** Radiation corrected radial temperature profiles with error bars at several axial positions.

wall heat transfer, which in turn leads to a 70 K lower maximum temperature. This temperature difference between the axial positions remains throughout the combustion chamber until the flue gas reaches the cooling coils.

Although the physical cooling coil entrance is located at 60 mm, the cooling effect can be detected 10 mm upstream. This effect arises from the big temperature difference between the burnt gas and the cooling coils and low gas velocities, such that heat conduction opposite to the flow direction becomes important. Interestingly, the effect of the cooling coils was observed to occur earlier for the upper position. Compared to the center and lower position, it shows a similar temperature trend slightly shifted by around 4 mm in radial direction. This observation was found to originate from the position of the cooling coil packages, which could not be perfectly aligned with respect to the burner surface due to manufacturing tolerances. This led to slightly varying cooling coil entry positions.

Concluding the temperature measurements, it has to be noted that this commercial condensing burner exhibits spatial temperature variations within its cylindrical heating unit, which remain throughout the combustion chamber until the flue gas is cooled by the cooling coils.

#### 4.3. CO species measurements

Due to very long measurement times of the gas chromatograph, which requires 30 min per measurement point, only three single measurement realizations of each profile at each axial position have been performed. On the left side in Fig. 8, the three measured radial profiles of the center location are displayed. Even though the trend for all realizations is similar, the deviations between these three profiles is significant and can account for 45% of the measured value. Compared to this, the method-induced measurement error only amounts to 3% of the measured concentration. From these different realizations, averaged profiles are derived and the large deviations between the different realizations result in large error bars, which now consider the method-induced measurement error along with the standard deviation between the different realizations.

On the right side of Fig. 8, the averaged CO profiles for the three axial positions are illustrated to study the impact of the detected temperature fluctuations in the burnt gas on the CO emissions. Despite the already explained large uncertainties of measured concentrations in the burnt region, a clear trend for the axial positions that exceeds these uncertainties could be observed. The highest concentrations of CO with 300 ppm were measured at the center position, while with 218 and 152 ppm significantly less CO was detected for upper and lower positions, respectively. Besides this, all profiles show an almost constant decrease of CO concentration until 65 mm. From there on, the CO mole

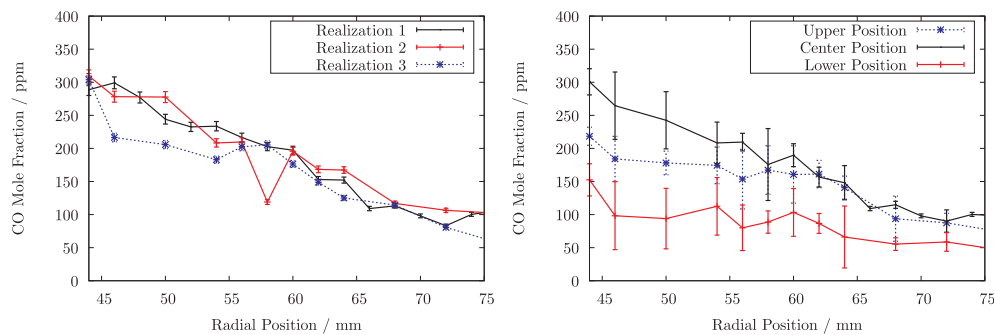


**Fig. 8.** Radial profiles from CO species measurement via gas chromatography (GC). Left: Different realizations at center position. Right: Averaged profiles at upper, center and lower axial position.

fraction remains approximately constant throughout the coil gap. This noteworthy amount of CO emissions in the cooled flue gas indicates the expected effect that the CO oxidation reactions freeze.

Regarding the CO concentration along with corresponding temperature profile at each axial position, a correlation between both quantities can be drawn. At the center position, the highest CO concentrations correlate with the highest measured temperatures. Consequently, the lowest CO concentrations are obtained at the lower position, where also the lowest temperatures have been measured.

#### 4.4. NO species measurements

As a third quantity, radial profiles of NO were measured to study the homogeneity of the condensing boiler system with respect to NO emissions. Fig. 9 shows the results of the performed chemiluminescence measurements. Different NO concentration levels have been measured at the three axial positions, showing the same inhomogeneous behavior as the temperature and CO measurements. The difference between the highest and the lowest measured NO concentration profile amounts to 45 %, indicating that the system is less homogeneous than originally supposed. The maximum of 21 ppm was detected at the center position, while the lowest concentrations have been measured at the upper axial position. Generally, the absolute concentration levels are close to the detection threshold of the measurement technique, which is also reflected in the relatively high error bars in Fig. 9.

Regarding the NO profiles in more detail, it is apparent that most of the NO is formed within the first 15 mm, with the steepest slope at the flame front location. From 15 mm on, the NO profiles do not show a clear trend. The highest measured NO concentrations at the center position slightly decrease in radial direction, while the lowest measured concentrations of the upper position slightly increase. A probable

explanation could be mixing effects, but this cannot be finally accessed due to relatively high measurement uncertainties.

The fact that most NO is formed within the flame front is interesting, since NO formation generally takes place on long timescales. However, the residence time of the gas in the flame front for the studied system is small, but increases with further radial distance due to continuity. From this, it can be concluded that the NO production rate in the flame front is significantly larger than in the postflame region to compensate for the low residence time. This demonstrates that the NO formation is not exclusively linked to the local gas temperature, which reaches its peak in the flame front at 6–8 mm away from the burner surface and remains constant in the postflame region. In contrast to that, the slope of NO concentration in the high temperature postflame region is very small, which indicates that high temperature levels alone do not enable NO formation reactions. Regarding the flue gas cooling, which starts at around 50 mm, no significant effect on the NO concentration is apparent.

Concluding the performed experimental measurements, the investigated quantities temperature, CO, and NO concentration exhibit noteworthy spatial fluctuations depending on the axial measurement position. The temperature variations are comparably small compared to higher fluctuations in the CO and NO emission levels. A temperature dependency, especially for the CO concentration, could be derived from the measured profiles. To examine the temperature dependency of CO and NO and to obtain a deeper understanding of their formation pathways in the examined condensing gas boiler system, resolved simulations with finite rate chemistry will be performed in the following.

#### 5. Numerical results

Multiple simulations with different settings were performed, which are listed in Table 3. First, the geometry abstraction is verified by comparing the circular hole with the slot case at the center position (case A & B). Afterwards, the effect of radiation heat losses is examined by applying the OTG and the DO model in the slot configuration at the center position (case C & D). Then, the effect of varying inlet velocities is studied by considering the upper and lower position (case E & F). Finally, the sensitivity with respect to the burner surface temperature is

**Table 3**  
Overview of performed simulations with the corresponding settings.

Case	Position	Hole Representation	Radiation	$T_{\text{burner}}$
A	Center	Circular hole (3D)	None	600 K
B	Center	Slot (2D)	None	600 K
C	Center	Slot (2D)	OTG	600 K
D	Center	Slot (2D)	DO	600 K
E	Upper	Slot (2D)	DO	600 K
F	Lower	Slot (2D)	DO	600 K
G	Center	Slot (2D)	DO	500 K
H	Center	Slot (2D)	DO	700 K

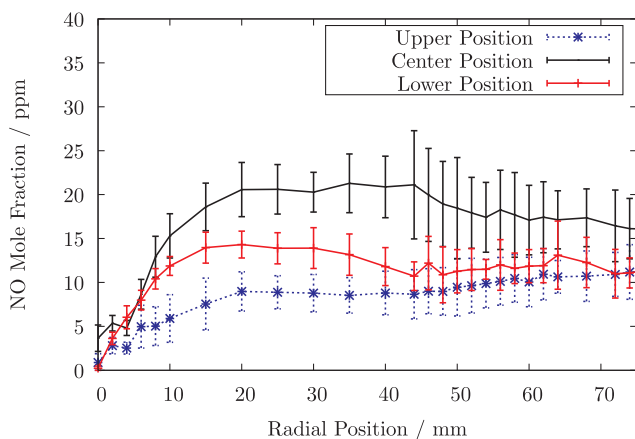


**Fig. 9.** NO species measurement utilizing probe sampling and chemiluminescence detector (CLD) analysis at several axial positions.



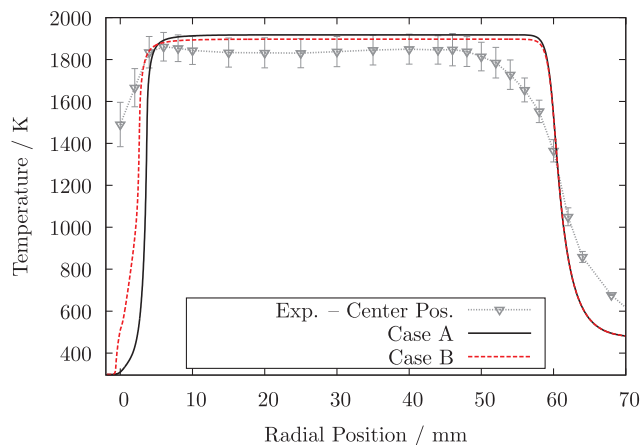


**Fig. 10.** Temperature comparison of the circular hole (case A) and slot geometry (case B) cases with the experimental measured temperature profile at the center position.

evaluated within a parameter study (case G & H).

### 5.1. Geometry abstraction

First, the impact of neglecting the circumferential direction by representing the actual circular burner hole by a simple slot is investigated. The corresponding results of cases A and B are illustrated in Fig. 10. Closely behind the burner hole, the velocity profiles of case A and B differ leading to different flame structures and lift-off lengths. These differences impact the wall heat transfer causing a deviation of the temperature in the postflame zone of 1.05%. The temperature gradients at the cooling coil entry are identical for both cases.

Comparing the simulation results with the measured temperature profile at the center position, it is found that the lift-off length of the slot geometry (case B) agrees better with the experimental temperature than the resolved circular hole (case A). This could originate from differences in the estimated inlet velocity used in the simulation compared to the actual velocity at the investigated burner location in the experiment.

Close to the burner surface, the measured temperature largely exceeds the temperature obtained from the simulation. As already noted, the dimensions of the used thermocouple prevent to resolve the temperature gradients in axial direction close to the burner surface. This makes it difficult to compare the experimental measured temperature with the simulation results of the burner hole's centerline.

In the postflame region, the temperature level of cases A & B are located at the upper uncertainty limit of the experimentally measured temperature. At cooling coil entry, the experimentally determined temperature slope is not as steep as in the simulation. Possible reasons could be the stagnation flow at the thermocouple tip or an inhomogeneous temperature distribution in the solid cooling coils, which is not represented by the approximated average coil temperature in the simulation.

### 5.2. Radiation effects

Regarding the experimental temperature profile in the postflame region in Fig. 10, no significant decrease along the radial pathway could be observed. This already suggests, that radiation heat losses do not play a major role in the studied system. This observation stands in contrast to findings in literature, where radiative heat transfer was denoted as an important effect [13,15,16]. To support the experimental result on gas radiation, two further cases were simulated, which apply the widely used optically thin gas (OTG) model and the more detailed discrete ordinate (DO) model (cases C & D).

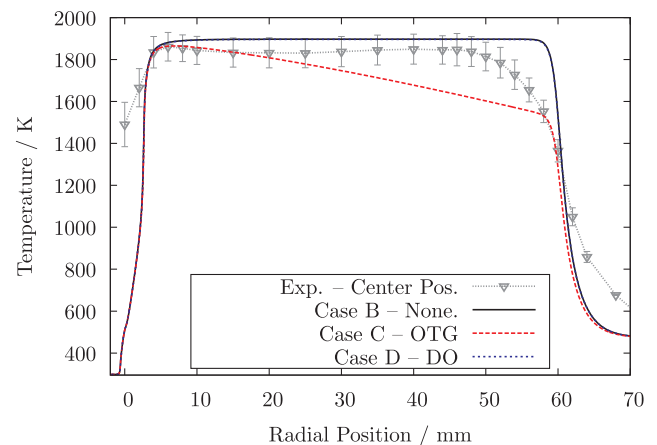


**Fig. 11.** Temperature comparison of the OTG (case C) and DO (case D) models with case B without a radiation model and the experimental measured temperature profile at the center position.

The corresponding results in Fig. 11 illustrate a large overestimation of radiative losses by the OTG model. Due to the simplicity of the OTG model, radiation energy is lost in all spatial directions. However, in the actual setup the radiation energy emitted by the hot flue gas can only be transferred to the solid burner and cooling coil and to the cold gas in the solids' vicinity. Moreover, the OTG model neglects the radiation absorption ability of the gas, which becomes important for long beam lengths [16].

For the DO case, the boundary conditions are defined such that radiation heat is only lost to the cold burner and cooling coil walls, but this effect is not influencing the temperature profile at the centerline considerably. Due to the low temperature level of the burner surface at the investigated nominal load point, the solid walls of the burner do not emit relevant amounts of radiation. It can be concluded that the net radiative heat transfer effect is marginal in the investigated heating unit.

### 5.3. Effect of varying boundary conditions

The measurements revealed different temperature levels for the measured positions (upper, center, lower). Possible reasons for this inhomogeneity are varying burner hole exit velocities and burner wall temperatures, which both impact the heat flux to the burner surface.

First, the influence of varying inlet velocities is studied by considering the upper and lower axial position, which have been examined in the experiments. The simulation results in Fig. 12 show a slightly different lift-off length in accordance to the defined inlet velocity, but the temperature level in the postflame region differs only marginally by 16 K in contrast to the variations of 90 K, which were found in the experiments. Also the observed temperature slope at the cooling coil entry is nearly similar for the three positions in the simulation. This indicates, that the burner hole exit velocity is not the main reason for different postflame temperature levels, which have been observed in the experiment.

To study the effect of gas preheating and wall heat losses on the temperature, the burner surface temperature was varied by  $\pm 100$  K in case G and H, based on the original burner temperature of 600 K to assess the sensitivity toward this relatively uncertain parameter. Fig. 13 shows that higher burner surface temperatures cause an increased preheating of the unburnt gas and reduce the wall heat losses of the burnt gas. Consequently, an increase of the burner wall temperature of 100 K leads to a difference in the flame temperature of roughly 50 K. While case G with a burner wall temperature of 500 K matches the experiments much better in the postflame region than the approximated value of 600 K, a wall temperature of 700 K (case H) clearly exceeds the



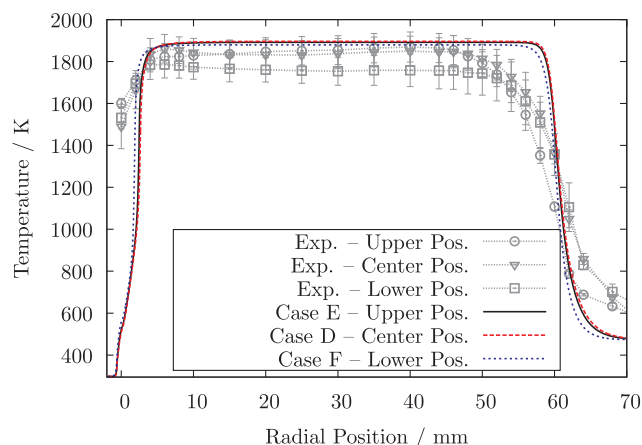


Fig. 12. Temperature profiles of the upper, center and lower axial position of the simulation (Case E, D & F) and the experimentally measured temperature profiles.

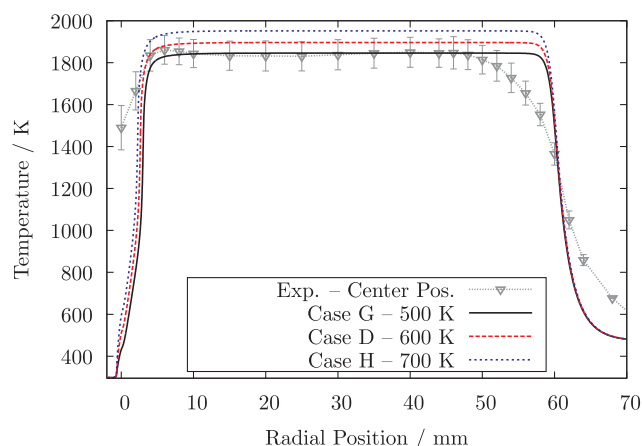


Fig. 13. Temperature profiles of varying burner surface temperatures (Case G, D & H) along with the experimentally measured temperature profile at the center position.

experimental temperature.

#### 5.4. CO emissions

Fig. 14 illustrates the course of the carbon monoxide (CO) mole fraction in radial direction of case A along with the experimentally measured profile. For the simulation, a CO peak value of 25,000 ppm can be found in the flame front, which quickly drops to 254 ppm in the postflame region due to oxidation reactions. From 25 mm on, until the gas approaches the cooling coils, the CO mole fraction remains constant, even though enough OH radicals are available for further oxidation. This indicates that CO has approached its chemical equilibrium, which was also confirmed by chemical equilibrium simulations utilizing the tool GasEQ<sup>1</sup> [41]. The level of the CO mole fraction in the postflame region predicted by the simulation agrees very well with the experiment, even though the experiment shows a slightly decreasing trend with high uncertainties due to the low number of measurement realizations. At the point of coil entry, the simulated CO mole fraction exhibits an instantaneous drop to 101 ppm. Afterwards, the CO concentration again remains on a constant level, which matches the experimentally measured values very well.

<sup>1</sup> The fundamentals of GasEQ are based on the complex, balanced chemical calculations defined by Sanford Gordon and Bonnie J. McBride for NASA.

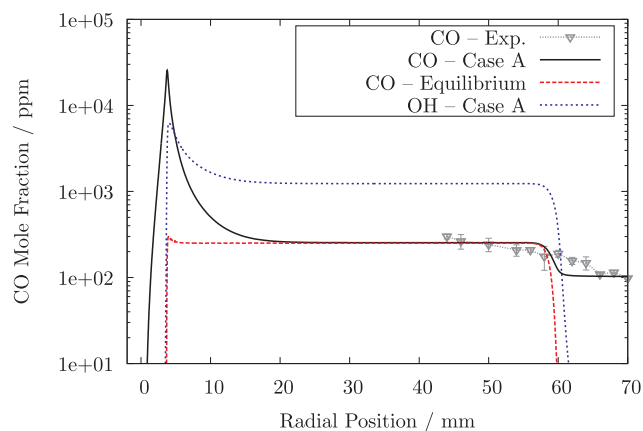


Fig. 14. Profiles of CO and OH mole fraction of the simulation case A, along with the equilibrium CO mole fraction from GasEQ simulations and the experimentally measured profile at the center position.

When the flue gas is cooled down by the cooling coils, the CO equilibrium concentration of reaction (5) shows a steep drop to a very small value. According to the principle of Le Chatelier, the equilibrium of this exothermic reaction shifts towards higher CO<sub>2</sub> and nearly zero CO concentrations for lower gas temperatures. However, the remaining CO mole fraction in the cooled flue gas is far higher than nearly zero equilibrium concentration. The reason for this quenching of the CO oxidation reaction, observed in the simulation and the experiment, can be found in a fast depletion of radicals by recombination reactions like (6) or (7). This effect has already been shown by Creighton [24]. He observed, that CO quenching is particularly sensitive to the gas cooling temperature gradient. From this, it can be stated that the CO emissions at the coil outlet depend on the equilibrium CO concentration before the gas enters the coils, which is a function of the temperature level in the postflame region. Additionally, the relaxation time characterizes how fast the flue gas is cooled down, which is in turn a function of the gas velocity.

#### 5.5. NO<sub>x</sub> formation

The formation of nitrogen oxide of case A is investigated and compared to the experimentally measured mole fraction profile in Fig. 15. The simulated NO profile shows a steep increase at the flame front position to 13 ppm, which can also be seen in the experiment. This steep increase points to a very high NO production rate in the flame front, which cannot be explained by the high temperature exclusively, because the temperature remains on that high level throughout the postflame region until the cooling coils are reached. The reason for this high NO production rate in the flame front originates from large concentrations of H, OH and O radicals in combination with high temperatures.

In the postflame region, the simulation predicts a further continuous increase of the NO mole fraction up to 26 ppm. However, the slope is much smaller compared to the flame front, despite the higher residence time in the postflame region. The reason for this reduced NO production rate is found in much lower radical concentrations, which have been consumed to a large extent within the flame front. The continuous NO production in the postflame region shows that the chemical equilibrium is not yet reached according to the simulation.

This trend cannot be confirmed by the experiment, which shows a rather constant or even a slightly decreasing development of NO in the postflame region. These diverging trends can be explained by the slight overestimation of the temperature level in the simulation due to too high burner surface temperatures. However, absolute concentration values of simulation and experiment agree quite well.

To comprehensively investigate the NO<sub>x</sub> emissions, which

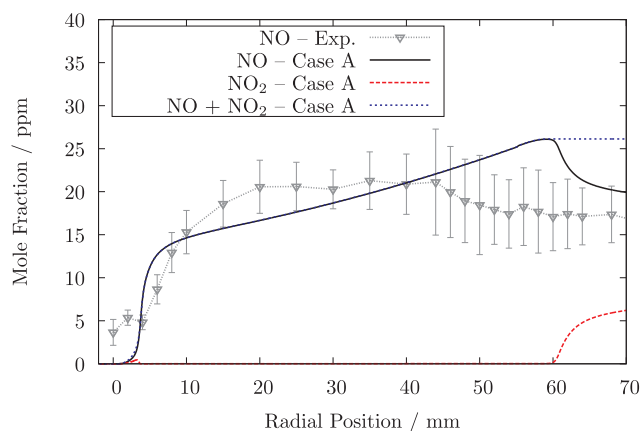


Fig. 15. Profiles of NO, NO<sub>2</sub> and NO<sub>x</sub> mole fraction of the simulation case A along with the experimentally measured profile at the center position.

represents the sum of NO and NO<sub>2</sub> concentrations, in the condensing gas boiler, the formation of NO<sub>2</sub> needs to be considered. However, the experimental chemiluminescence detector is only capable of measuring NO. Consequently, the NO<sub>2</sub> profile can just be evaluated numerically. Here, the simulation predicts the formation of small fractions of NO<sub>2</sub> (1 ppm) in the flame front, which are quickly consumed downstream. When the flue gas is cooled down by the cooling coils, the NO production stops and an oxidation reaction becomes relevant, which oxidizes NO and forms NO<sub>2</sub>. However, the sum of NO and NO<sub>2</sub> mole fraction, i.e. the NO<sub>x</sub> mole fraction, remains on a constant level in the cooled flue gas.

This oxidation reaction could also be the cause for decreasing NO concentrations in the postflame region in the experiment, which can already be observed before the gas reaches the cooling coils. The end of the steel tubing used for probe sampling is cooled down by the cooling coils, which also decreases the tip temperature of the tubing due to the high thermal conductivity of steel. Consequently, NO is oxidized to NO<sub>2</sub> within the tubing before it reaches the detector.

Fig. 16 displays the NO net production rate near the flame front, which shows maximum values in the flame front. This was already expected, because the NO profile showed a steep rise in the flame front in Fig. 15. In the postflame region, the production rate decreases significantly. Splitting the total NO net production rate into its four contributions, the net production rates of the thermal, prompt, NNH, and N<sub>2</sub>O pathways can be obtained, which are illustrated in Fig. 17. To analyze the net production rates more quantitatively, their profiles along the radial centerline are shown in Fig. 18. The thermal pathway shows relatively low net formation rates in the flame front, but it is still active in the postflame region and causes the slight but continuous increase of NO from 10 mm to 60 mm in Fig. 15. To calculate the overall contribution, the net production rate is integrated over the volume and normalized with the total net production rate of NO:

$$X_{\text{thermal}} = \frac{\int \dot{c}_{\text{NO,thermal}} dV}{\int \dot{c}_{\text{NO,total}} dV}. \quad (8)$$

From this, an overall contribution of 35.3% for the thermal pathway can be assigned.

The prompt pathway shows the highest local production rates, but it is only active within the flame front, because the required CH radicals are only available in this region. Its overall contribution to the NO formation adds up to 13.5%, which is the lowest contribution of all formation pathways.

Regarding the NNH pathway in Figs. 17 and 18, high net production rates can be found in and closely behind the flame front. The combination of high net production rates present within a larger volume results in an overall contribution of 31.5%. With this, the NNH pathway presents the second most important pathway in the total NO formation.

At last, the N<sub>2</sub>O pathway is considered, which shows a moderate level of NO production in the flame front, but also a small amount of backward reactions ahead of the flame front in Fig. 17. Fig. 18 displays a small contribution in the postflame region, which is one order of magnitude smaller than the net production rate of the thermal pathway. While the thermal production rate is rapidly dropping due to decreasing temperatures when the gas approaches the cooling coils, a sudden increase of the N<sub>2</sub>O production rate occurs, as can be seen in Fig. 18. However, with further decreasing temperatures causing a depletion of all available radicals, the production rate of the N<sub>2</sub>O pathway also drops to zero 1 mm further downstream. Its overall contribution amounts to 19.7%.

## 6. Summary and conclusion

In this study, the cylindrical heating unit of a full-scale condensing gas boiler was investigated experimentally and numerically with respect to the temperature level as well as the formation of the emission species CO and NO. The experimental measurements revealed an inhomogeneous distribution of these quantities depending on the axial measurement location. In the temperature measurements, gas radiation effects were found to be marginal due to the closed system design. Regarding the CO measurements, noteworthy amounts of CO remain in the cooled flue gas confirming the expected oxidation freezing effect.

The numerical investigations were based on resolved simulations of a single burner hole applying finite rate chemistry. A sensitivity study showed that varying burner surface temperatures affect the temperature level in the postflame region more than varying inlet velocities. From this study, a burner surface temperature of 500 K was identified to be the most reasonable surface temperature as this simulation case showed the best agreement with the experimental results.

For the current setup, the optically thin gas radiation model significantly overestimated radiative heat losses. In contrast, the more detailed discrete ordinate model from Liu et al. [34] showed much better agreement with the experimental data and illustrated that radiative heat losses are marginal in the investigated system at nominal operating conditions.

Regarding the CO profiles and emissions predicted by the simulation, the CO concentration was found to quickly reach its temperature dependent equilibrium concentration in the postflame region. When the hot flue gas is cooled down by the cooling coils, first the CO concentration strongly decreases due to oxidation to CO<sub>2</sub>, but then the radical concentrations quickly drop, such that the CO oxidation reactions are frozen. Thus, noteworthy amounts of CO remain in the flue gas, even though the CO equilibrium concentration would be essentially zero at this temperature level. The effect of CO oxidation freezing

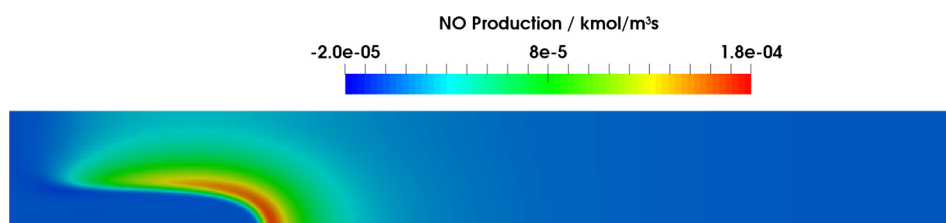


Fig. 16. Net production rate of nitrogen oxide in the centerplane from 0 mm until 10 mm behind the burner.

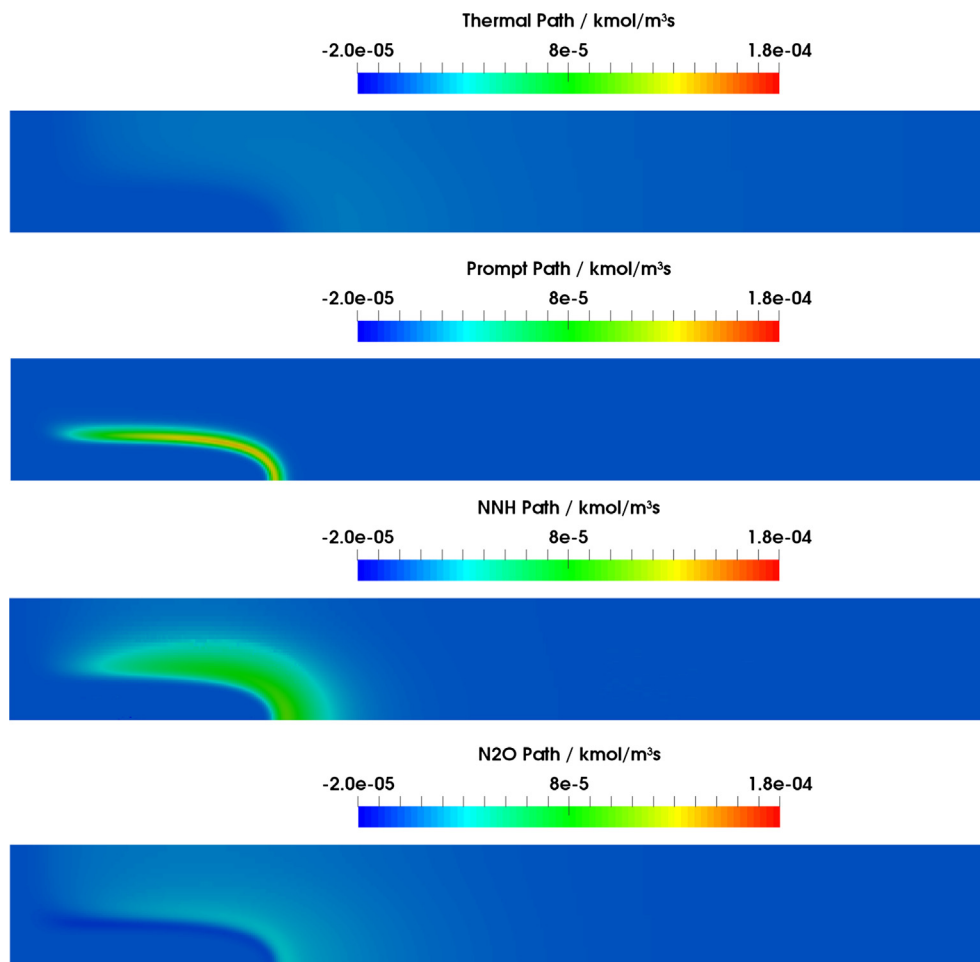


Fig. 17. NO net production rate split according to the four different formation pathways in the centerplane from 0 mm until 10 mm behind the burner.

explains the noted phenomena that the load-normalized CO emissions reach their maximum level at nominal load. At such high load points, the gas mass flows and velocities are higher than for lower loads leading to steeper cooling gradients at coil entry and a freeze of the CO concentration on higher levels. While previous studies tried to reduce CO emissions by measures affecting the flame itself, this new finding highlights that CO emissions can be reduced more efficiently at the heat exchanger stage by flattening the cooling gradient of the flue gas. To lower gas velocities at coil entry, the cooling coils could be positioned further downstream in cylindrical configurations or the gap between the cooling coils could be slightly widened. However, these measures potentially increase the required installation space or impact the energy efficiency, which also needs to be considered in the development phase.

Finally, the four NO formation pathways, namely the thermal,

prompt, NNH and N<sub>2</sub>O pathway, have been studied. It was shown that even under lean conditions, the thermal pathway still has the highest contribution to the overall NO production. This indicates that there is some potential left to reduce the overall NO emissions by reducing the thermal NO formation. This could be achieved by leaner mixtures, exhaust gas recirculation, or enhanced radiative heat loss from the flame holder, as long as flame stability is still ensured. However, the approach to reduce NO emissions by achieving lower burnt gas temperature levels – as it is suggested in literature – is limited, because the other three NO formation pathways are not as temperature sensitive as the thermal pathway, but rely more on the radical concentration in the flame front. Therefore, other approaches have to be considered to further decrease NO emissions beyond that level.

By investigating a full-scale condensing gas boiler device, an

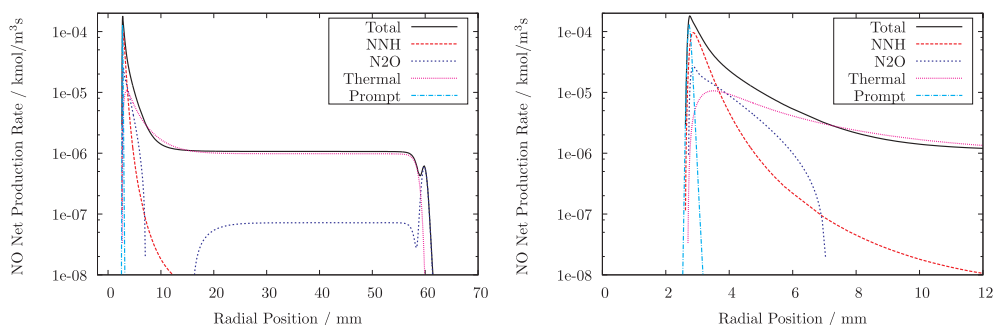


Fig. 18. Radial profiles of NO pathway net production rates along radial direction (left). Right: Enlarged view of profiles in the vicinity of the burner.

inhomogeneous temperature field was found due to locally varying burner exit velocities. Locally increased temperature levels cause much higher CO and NO emissions in these regions due to the strong temperature sensitivity of their formation pathways. This needs to be addressed in future studies by investigating the flow field inside the multi-hole burner. Homogenizing the burner exit velocities would avoid these locally increased emission levels.

Concluding, measuring averaged species concentrations behind the heat exchanger represents a commonly applied procedure to reduce overall emission levels of condensing gas boiler devices. In the past, this procedure helped to identify emission reducing measures, which resulted in already very low pollutant emissions of the current boiler generation. However, further decreasing the emissions with this procedure is difficult due to a lack of knowledge on locally existing high

emission regions and the exact formation pathways of regulated pollutants. Consequently, detailed local measurements and simulations are required to identify such critical regions as it was demonstrated in this study. To be aware of these regions along with the knowledge on the relevant formation pathways open up possibilities to develop new measures for next condensing boiler generations.

## Acknowledgements

The authors from RWTH Aachen University gratefully acknowledge funding from Vaillant GmbH. Computations were performed with computing resources granted by JARA-HPC from RWTH Aachen University under project jara0139.

## Appendix A

See Fig. 19.

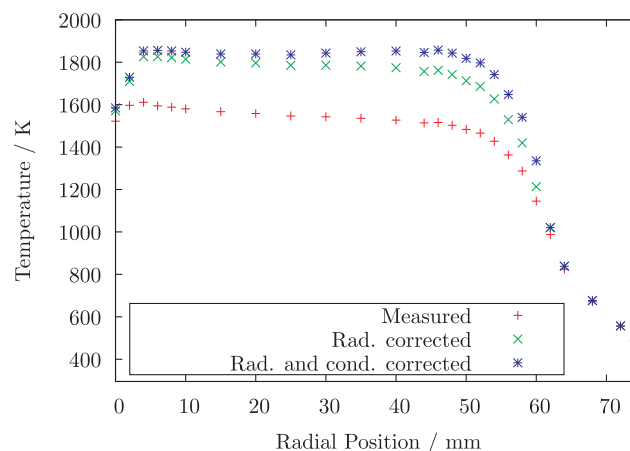


Fig. 19. Measured temperature, temperature including radiation correction term, and temperature containing radiation and heat conduction correction term.

## References

- [1] der Deutschen Heizungsindustrie (BDH) B. Effiziente systeme und erneuerbare energien. Tech rep. Frankfurter Str. 720 - 726, 51145 Cologne, Germany; 2017. < <https://www.bdh-koeln.de/publikationen.html> > .
- [2] Weber C, Gebhardt B, Fahl U. Market transformation for energy efficient technologies - success factors and empirical evidence for gas condensing boilers. *Energy* 2002;27:287–315.
- [3] Johnson G, Beausoleil-Morrison I. The calibration and validation of a model for predicting the performance of gas-fired tankless water heaters in domestic hot water applications. *Appl Energy* 2016;177:740–50. <https://doi.org/10.1016/j.apenergy.2016.05.130> < <http://www.sciencedirect.com/science/article/pii/S0306261916307346> > .
- [4] Shang S, Li X, Chen W, Wang B, Shi W. A total heat recovery system between the flue gas and oxidizing air of a gas-fired boiler using a non-contact total heat exchanger. *Appl Energy* 2017;207:613–23. <https://doi.org/10.1016/j.apenergy.2017.05.169>. [transformative Innovations for a Sustainable Future – Part II]. < <http://www.sciencedirect.com/science/article/pii/S0306261917307262> > .
- [5] Chen Q, Finney K, Li H, Zhang X, Zhou J, Sharifi V, et al. Condensing boiler applications in the process industry. *Appl Energy* 2012;89(1):30–6. <https://doi.org/10.1016/j.apenergy.2010.11.020> [special issue on Thermal Energy Management in the Process Industrie]. < <http://www.sciencedirect.com/science/article/pii/S0306261910004836> > .
- [6] de Vries H, Mokhov AV, Levinsky HB. The impact of natural gas/hydrogen mixtures on the performance of end-use equipment: interchangeability analysis for domestic appliances. *Appl Energy* 2017;208:1007–19. <https://doi.org/10.1016/j.apenergy.2017.09.049> < <http://www.sciencedirect.com/science/article/pii/S0306261917313302> > .
- [7] McKenna R, Bchini Q, Weinand J, Michaelis J, Koenig S, Koeppel W, et al. The future role of power-to-gas in the energy transition: Regional and local techno-economic analyses in Baden-Wuerttemberg. *Appl Energy* 2018;212:386–400. <https://doi.org/10.1016/j.apenergy.2017.12.017> < <http://www.sciencedirect.com/science/article/pii/S0306261917317312> > .
- [8] Badr O, Probert S. Oxides of nitrogen in the earth's atmosphere: trends, sources, sinks and environmental impacts. *Appl Energy* 1993;46(1):1–67. [https://doi.org/10.1016/0306-2619\(93\)90076-2](https://doi.org/10.1016/0306-2619(93)90076-2) < <http://www.sciencedirect.com/science/article/pii/S0306261993900762> > .
- [9] Badr O, Probert S. Sinks and environmental impacts for atmospheric carbon monoxide. *Appl Energy* 1995;50(4):339–72. [https://doi.org/10.1016/0306-2619\(95\)98803-A](https://doi.org/10.1016/0306-2619(95)98803-A) < <http://www.sciencedirect.com/science/article/pii/S030626199598803A> > .
- [10] Gas-fired heating boilers - part 1: General requirements and tests, german version en15502-1:2012; 2012.
- [11] Gas-fired central heating boilers - part 2-1: Specific standard for type c appliances and type b2, b3 and b5 appliances of a nominal heat input not exceeding 1 000 kw; german version en 15502-2-1:2012; 2012.
- [12] Trimis D, Durst F. Combustion in a porous medium-advances and applications. *Combust Sci Technol* 1996;121(1–6):153–68. <https://doi.org/10.1080/00102209608935592>.
- [13] Bouma P, De Goey L. Premixed combustion on ceramic foam burners. *Combust Flame* 119 (1–2). [https://doi.org/10.1016/S0010-2180\(99\)00050-4](https://doi.org/10.1016/S0010-2180(99)00050-4).
- [14] Malico I, Zhou X, Pereira J. Two-dimensional numerical study of combustion and pollutants formation in porous burners. *Combust Sci Technol* 2000;152(1):57–79. <https://doi.org/10.1080/00102200008952127>.
- [15] Lammers F, de Goey L. A numerical study of flash back of laminar premixed flames in ceramic-foam surface burners. *Combust Flame* 2003;133(1):47–61. [https://doi.org/10.1016/S0010-2180\(02\)00540-0](https://doi.org/10.1016/S0010-2180(02)00540-0) < <http://www.sciencedirect.com/science/article/pii/S0010218002005400> > .
- [16] Lammers F, de Goey L. The influence of gas radiation on the temperature decrease above a burner with a flat porous inert surface. *Combust Flame* 2004;136(4):533–47. <https://doi.org/10.1016/j.combustflame.2003.12.010> < <http://www.sciencedirect.com/science/article/pii/S0010218004000070> > .
- [17] Mujeebu MA, Abdullah MZ, Bakar MZA, Mohamad AA, Abdullah MK. Applications of porous media combustion technology – a review. *Appl Energy* 2009;86(9):1365–75. <https://doi.org/10.1016/j.apenergy.2009.01.017> < <http://www.sciencedirect.com/science/article/pii/S0306261909000294> > .



- [18] Kedia KS, Ghoniem AF. Mechanisms of stabilization and blowoff of a premixed flame downstream of a heat-conducting perforated plate. *Combust Flame* 2012;159(3):1055–69. <https://doi.org/10.1016/j.combustflame.2011.10.014> <<http://www.sciencedirect.com/science/article/pii/S0010218011003191>> .
- [19] Konnov A, Riemeljeer R, Kornilov V, de Goeij L. 2d effects in laminar premixed flames stabilized on a flat flame burner. *Exp Therm Fluid Sci* 2013;47:213–23. <https://doi.org/10.1016/j.expthermflusci.2013.02.002> <<http://www.sciencedirect.com/science/article/pii/S0894177113000356>> .
- [20] Goswami M, Coumans K, Bastiaans RJM, Konnov AA, de Goeij L. Numerical simulations of flat laminar premixed methane-air flames at elevated pressure. *Combust Sci Technol* 2014;186(10–11):1447–59. <https://doi.org/10.1080/00102202.2014.934619>.
- [21] Lee S, Kum S-M, Lee C-E. An experimental study of a cylindrical multi-hole premixed burner for the development of a condensing gas boiler. *Energy* 2011;36(7):4150–7. <https://doi.org/10.1016/j.energy.2011.04.029> <<http://www.sciencedirect.com/science/article/pii/S0360544211002787>> .
- [22] Lee PH, Hwang SS. Formation of lean premixed surface flame using porous baffle plate and flame holder. *J Therm Sci Technol* 2013;8(1):178–89. <https://doi.org/10.1299/jtst.8.178>.
- [23] Lee S, Kim J-M, Kum S-M, Lee C-E. Suggestion on the simultaneous reduction method of CO and NOx in premixed flames for a compact heat exchanger. *Energy Fuels* 2010;24:821–7. <https://doi.org/10.1021/ef9008554>.
- [24] Creighton JR. Dependence of CO emissions on the rate of product cooling. *Combust Flame* 2000;123(3):402–11. [https://doi.org/10.1016/S0010-2180\(00\)00160-7](https://doi.org/10.1016/S0010-2180(00)00160-7) <<http://www.sciencedirect.com/science/article/pii/S0010218000001607>> .
- [25] Turns SR. An introduction to combustion - concepts and applications. 2nd ed. The McGraw-Hill Higher Education; 2000.
- [26] Trisjono P, Pitsch H. A direct numerical simulation study on NO formation in lean premixed flames. *Proc Combust Inst* 2017;36(2):2033–43. <https://doi.org/10.1016/j.proci.2016.06.130> <<http://www.sciencedirect.com/science/article/pii/S1540748916301882>> .
- [27] Shaddix CR. Correcting thermocouple measurements for radiation loss: a critical review. Tech rep. Livermore, CA (US): Sandia National Labs.; 1999.
- [28] Hindasageri V, Vedula R, Prabhu S. Thermocouple error correction for measuring the flame temperature with determination of emissivity and heat transfer coefficient. *Rev Sci Instrum* 2013;84(2):024902.
- [29] Liu D, Togbé C, Tran L-S, Felsmann D, Oßwald P, Nau P, et al. Combustion chemistry and flame structure of furan group biofuels using molecular-beam mass spectrometry and gas chromatography - part I: Furan. *Combust Flame* 2014;161(3):748–65. <https://doi.org/10.1016/j.combustflame.2013.05.028> [special Issue on Alternative Fuels]. <<http://www.sciencedirect.com/science/article/pii/S0010218013002216>> .
- [30] Desjardins O, Blanquart G, Balarac G, Pitsch H. High order conservative finite difference scheme for variable density low mach number turbulent flows. *J Comput Phys* 2008;227(15):7125–59. <https://doi.org/10.1016/j.jcp.2008.03.027> <<http://www.sciencedirect.com/science/article/pii/S0021999108001666>> .
- [31] Blanquart G, Pepiot-Desjardins P, Pitsch H. Chemical mechanism for high temperature combustion of engine relevant fuels with emphasis on soot precursors. *Combust Flame* 2009;156(3):588–607. <https://doi.org/10.1016/j.combustflame.2008.12.007> <<http://www.sciencedirect.com/science/article/pii/S0010218008003957>> .
- [32] Smith GP, Golden DM, Frenklach M, Moriarty NW, Eiteneer B, Goldenberg M, et al. <[http://www.me.berkeley.edu/gri\\_mech/](http://www.me.berkeley.edu/gri_mech/)> .
- [33] Bowman CT, Hanson RK, Davidson DF, et al. GRI-Mech 2.11; 1995. <[http://www.me.berkeley.edu/gri\\_mech/](http://www.me.berkeley.edu/gri_mech/)> .
- [34] Liu F, Guo H, Smallwood GJ. Effects of radiation model on the modeling of a laminar coflow methane/air diffusion flame. *Combust Flame* 2004;138(1):136–54. <https://doi.org/10.1016/j.combustflame.2004.04.007> <<http://www.sciencedirect.com/science/article/pii/S0010218004000963>> .
- [35] Strang G. On the construction and comparison of difference schemes. *SIAM J Numer Anal* 1968;5(3):506–17. <https://doi.org/10.1137/0705041>.
- [36] Brown PN, Byrne GD, Hindmarsh AC. Vode: a variable-coefficient ode solver. *SIAM J Sci Stat Comput* 1989;10(5):1038–51. <https://doi.org/10.1137/0910062>.
- [37] HYPRE software package. Lawrence Livermore National Laboratory. Available at <<http://computation.llnl.gov/casc/hypre/software.html>> .
- [38] Jiang G-S, Shu C-W. Efficient implementation of weighted ENO schemes. *J Comput Phys* 1996;126(1):202–28. <https://doi.org/10.1006/jcph.1996.0130> <<http://www.sciencedirect.com/science/article/pii/S0021999196901308>> .
- [39] Bosschaert K, de Goeij L. The laminar burning velocity of flames propagating in mixtures of hydrocarbons and air measured with the heat flux method. *Combust Flame* 2004;136(3):261–9. <https://doi.org/10.1016/j.combustflame.2003.10.005> <<http://www.sciencedirect.com/science/article/pii/S001021800300275X>> .
- [40] Goswami M, Derks SC, Coumans K, Slikker WJ, de Andrade Oliveira MH, Bastiaans RJ, et al. The effect of elevated pressures on the laminar burning velocity of methane + air mixtures. *Combust Flame* 2013;160(9):1627–35. <https://doi.org/10.1016/j.combustflame.2013.03.032> <<http://www.sciencedirect.com/science/article/pii/S0010218013001326>> .
- [41] Morely C. GASEQ version 0.79; 2016. <<http://www.arcl02.dsl.pipex.com>> .